Deterministic and storable single photons from a multilayer microsphere

Tuan Anh Nguyen and Ho Trung Dung
Insitute of Physics, Academy of Sciences and Technology, 1 Mac Dinh Chi Street, District 1, Ho Chi Minh city, Vietnam
(Received 12 December 2006; published 27 September 2007)

We consider the generation of single photons on demand by pumping an emitter which is enclosed within a spherical distributed dielectric resonator, and then letting it emit spontaneously. The three-dimensional confinement in space of the electromagnetic field gives rise to deep dips and high peaks in the spectral profile of the density of states. The dips can be made use of to store the excitation energy and the peaks to narrow the time window during which a photon is emitted. The feasibility of the proposed scheme is discussed.

DOI: 10.1103/PhysRevA.76.033831 PACS number(s): 42.70.Qs, 85.60.Jb, 42.25.Bs, 42.50.Pq

I. INTRODUCTION

The availability of single-photon sources holds the key to new and powerful techniques in quantum information processing, quantum key distribution, metrology, and fundamental tests of quantum mechanics [1,2]. The design of these sources is a challenging task and is currently an active area of research. Ideally, a single-photon source emits precisely one indistinguishable photon, with unit fidelity and high repetition rate, into a known spatiotemporal mode at a known moment of time. Depending on applications, many demands can be relaxed. For example, any source that furnishes an appropriately polarized photon within a prescribed time window is fit for quantum key distribution. One way by which single photons may be produced is via the spontaneous emission from individually addressable quantum emitters. Within the emitter upper-state lifetime and the emission solid angle—almost omnidirectional in free space—the process is inherently random. This can be mitigated by tailoring the surrounding environment so as to facilitate the atomic coupling to a single spatial mode of the electromagnetic field. Experiments in this direction have been carried out using planar distributed Bragg reflectors [3,4], pillar microcavities [5,6], and curved high-finesse cavities [7].

More flexibility can be injected into a single-photon on-demand source by temporally separating the excitation and the emission process. This can be achieved by pumping the emitter while the transition to the ground state is turned off. When needed, this transition can be switched on to trigger a photon generation. Schemes based on photonic band-gap structures with the switching mechanism being a Kerr nonlinearity have been considered in Refs. [8,9]. A tunable on-chip micromaser using a superconducting quantum circuit as an artificial atom with externally controllable state transitions has been suggested in Ref. [10]. Related schemes where single photons generated by Raman scattering of a write pulse and stored in an atomic ensemble are released by a read pulse after a programable time delay, were examined experimentally in Ref. [11]. Photon storage in a loop may also help to make a spontaneous parametric down-conversion source deterministic [12].

In Refs. [2,8,9], desired modifications to the spontaneous emission process are achieved by surrounding the emitter with photonic band-gap crystals. In band-gap crystals of planar type, the confinement of the electromagnetic field is only in one dimension. In systems with spatial periodicity in all three dimensions, it is difficult to control the periodicity of the material over large length scales. An alternative route to realize a single-mode atom-field coupling, which will be considered here, is to rely on isolated dielectric particles with radially periodic quarter-wave modulation in refractive index. Although such spherical distributed layers lack a translational invariance and are not band-gap structures in a rigorous sense, they can inhibit light propagation over a complete solid angle and finite frequency ranges, and give rise to the existence of very sharp resonances [13–15]. The spherical distributed resonator offers additional advantages that its Green tensor is exactly known [16,17] and that it now can be fabricated in the laboratories with relative ease using various techniques including electron-beam deposition [18], etching combined with chemical-vapor deposition [19], multistage emulsion polymerization [20], or thermal printing [21]. Contrasts of refractive indices as high as 3.5 (Si) versus 1.5 (SiO_2) have been reported [20]. Certain features of the spontaneous emission rate in such structures have been investigated theoretically [22].

Here we propose a prototype for a single-photon on-demand gun, based on enclosing an individually addressable emitter in a spherical distributed resonator. The article is organized as follows. In Sec. II, general formulas are given. Section III is devoted to a numerical analysis of general characteristics of the spontaneous decay process, including the decay rate, the emission pattern, and the amount of radiation energy. The merits of using the spontaneous decay of an emitter enclosed within a spherical distributed resonator as a core process in a single-photon emitting device are discussed in Sec. IV. The article ends with a summary in Sec. V.

II. BASIC FORMULAS

A. Arbitrary geometry

Consider an electric dipole emitter (position $\mathbf{r}_A$, transition frequency ω_A, transition dipole moment $\mathbf{d}_A$) in the presence of arbitrary, dispersing, and absorbing bodies. We assume that the emitter has appropriate energy level configuration and is small enough in size so that the electric-dipole approximation applies, and that the emitter-electromagnetic field interaction is in the weak coupling regime. Its spontaneous decay rate can then be determined according to the formula [23,24]

$$\Gamma = \frac{2k_A^2}{\hbar\varepsilon_0}\mathbf{d}_A \,\mathrm{Im}\,\mathbf{G}(\mathbf{r}_A,\mathbf{r}_A,\omega_A)\mathbf{d}_A, \tag{1}$$

where $k_A=\omega_A/c$ and $\mathbf{G}(\mathbf{r},\mathbf{r}',\omega)$ is the (classical) Green tensor of the medium-assisted Maxwell field. Note that ω_A already includes the medium-induced level shift.

The spatial pattern of the emitted light can be determined via the intensity of the light registered by a pointlike photodetector at position $\mathbf{r}$ and time t [24]

$$I(\mathbf{r},t) = |\mathbf{F}(\mathbf{r},\mathbf{r}_A,\omega_A)|^2 e^{-\Gamma t}, \tag{2}$$

where, after discarding a small nonresonant term,

$$\mathbf{F}(\mathbf{r},\mathbf{r}_A,\omega_A) \simeq \frac{-ik_A^2}{\varepsilon_0}\mathbf{G}(\mathbf{r},\mathbf{r}_A,\omega_A)\mathbf{d}_A. \tag{3}$$

The expectation value of the radiation energy transported through an area $\mathcal{A}$ can be expressed in terms of the Poynting vector as

$$W_{\mathcal{A}} = \int_0^\infty dt \int_{\mathcal{A}} d\mathbf{a}\cdot\mathbf{S}(\mathbf{r},t), \tag{4}$$

where $\mathbf{S}(\mathbf{r},t)$ is the Poynting vector [9]

$$\mathbf{S}(\mathbf{r},t) = \frac{2\omega_A^3}{\varepsilon_0 c^2}\,\mathrm{Im}\{[\mathbf{G}^*(\mathbf{r},\mathbf{r}_A,\omega_A)\mathbf{d}_A] \times [\boldsymbol{\nabla}\times\mathbf{G}(\mathbf{r},\mathbf{r}_A,\omega_A)\mathbf{d}_A]\}e^{-\Gamma t}. \tag{5}$$

In particular, when the area $\mathcal{A}$ is a part of a spherical surface $d\mathbf{a}=d\phi d\theta\sin\theta r^2\mathbf{e}_r$, and Eq. (4) leads to

$$W_{\mathcal{A}} = \int_{\mathcal{A}} d\Omega W(\Omega) = \int_{\mathcal{A}} d\theta\sin\theta\int_{\mathcal{A}} d\phi W(\Omega), \tag{6}$$

where

$$W(\Omega) = \int_0^\infty dt r^2\mathbf{e}_r\cdot\mathbf{S}(\mathbf{r},t) \tag{7}$$

is the expectation value of the radiation energy emitted per unit solid angle [9].

Regarding $\mathcal{A}$ as a closed spherical surface in the far-field zone, $W_{\mathcal{A}}$ represents the total amount of radiation energy transported to the outside of the cavity W [9,24]

$$W = 2c\varepsilon_0\int_0^\infty dt\int_0^\pi d\theta\sin\theta\int_0^{2\pi} d\phi r^2 I(\mathbf{r},t). \tag{8}$$

To account for the local-field correction, we employ the real-cavity model and assume that the atom is surrounded by an empty spherical cavity of radius R_C, which represents an average distance from the emitter to the nearest constituents of the macroscopic body. The Green tensor of equal positions can then be separated into a bulk and a scattering part $\mathbf{G}^{(0)}$ and $\mathbf{G}^{(1)}_{\mathrm{loc}}$, respectively,

$$\mathbf{G}(\mathbf{r}_A,\mathbf{r}_A,\omega) = \mathbf{G}^{(0)}(\mathbf{r}_A,\mathbf{r}_A,\omega) + \mathbf{G}^{(1)}_{\mathrm{loc}}(\mathbf{r}_A,\mathbf{r}_A,\omega), \tag{9}$$

where the bulk part refers to free space, and the scattering part is [25,26]

$$\mathbf{G}^{(1)}_{\mathrm{loc}}(\mathbf{r}_A,\mathbf{r}_A,\omega_A) = \frac{k_A}{6\pi}\left\{\frac{3(\varepsilon-1)}{2\varepsilon+1}\frac{1}{(k_AR_C)^3} + \frac{9(\varepsilon-1)(4\varepsilon+1)}{5(2\varepsilon+1)^2}\frac{1}{k_AR_C} + i\left[\frac{9\varepsilon^{5/2}}{(2\varepsilon+1)^2}-1\right]\right\}\mathbf{I} + \left(\frac{3\varepsilon}{2\varepsilon+1}\right)^2 \times\mathbf{G}^{(1)}_{\mathrm{med}}(\mathbf{r}_A,\mathbf{r}_A,\omega_A) + O(k_AR_C), \tag{10}$$

$\varepsilon=\varepsilon(\mathbf{r}_A,\omega_A)$ and $\mathbf{I}$ is the unit tensor. For the Green tensor of different positions

$$\mathbf{G}_{\mathrm{loc}}(\mathbf{r},\mathbf{r}_A,\omega_A) = \frac{3\varepsilon}{2\varepsilon+1}\mathbf{G}_{\mathrm{med}}(\mathbf{r},\mathbf{r}_A,\omega_A) + O(k_AR_C). \tag{11}$$

In Eqs. (11) and (10), $\mathbf{G}_{\mathrm{med}}$ is the Green tensor in the absence of the emitter and the (real) cavity while $\mathbf{G}^{(1)}_{\mathrm{med}}$ is its scattering part.

Putting Eqs. (9) and (10) in Eq. (1), we obtain

$$\Gamma = \Gamma_0 + \Gamma_C + \Gamma^{(1)}, \tag{12}$$

where

$$\Gamma_0 = \frac{k_A^3 d_A^2}{3\pi\hbar\varepsilon_0} \tag{13}$$

is the free-space decay rate,

$$\Gamma_C = \Gamma_0\,\mathrm{Im}\left\{\frac{3(\varepsilon-1)}{2\varepsilon+1}\frac{1}{(k_AR_C)^3} + \frac{9(\varepsilon-1)(4\varepsilon+1)}{5(2\varepsilon+1)^2}\frac{1}{k_AR_C} + i\left[\frac{9\varepsilon^{5/2}}{(2\varepsilon+1)^2}-1\right]\right\}, \tag{14}$$

and

$$\Gamma^{(1)} = \frac{2k_A^2}{\hbar\varepsilon_0}\mathbf{d}_A\,\mathrm{Im}\left[\left(\frac{3\varepsilon}{2\varepsilon+1}\right)^2\mathbf{G}^{(1)}_{\mathrm{med}}(\mathbf{r}_A,\mathbf{r}_A,\omega_A)\right]\mathbf{d}_A. \tag{15}$$

Putting Eq. (11) in Eq. (3) leads to

$$\mathbf{F}(\mathbf{r},\mathbf{r}_A,\omega_A) \simeq \frac{-ik_A^2}{\varepsilon_0}\frac{3\varepsilon}{2\varepsilon+1}\mathbf{G}^{(1)}_{\mathrm{med}}(\mathbf{r},\mathbf{r}_A,\omega_A)\mathbf{d}_A \tag{16}$$

while using Eq. (11) in Eq. (5) yields

$$\mathbf{S}(\mathbf{r},t) = \frac{2\omega_A^3}{\varepsilon_0 c^2}\left|\frac{3\varepsilon}{2\varepsilon+1}\right|^2\mathrm{Im}\{[\mathbf{G}^*_{\mathrm{med}}(\mathbf{r},\mathbf{r}_A,\omega_A)\mathbf{d}_A] \times[\boldsymbol{\nabla}\times\mathbf{G}_{\mathrm{med}}(\mathbf{r},\mathbf{r}_A,\omega_A)\mathbf{d}_A]\}e^{-\Gamma t}. \tag{17}$$

B. Multilayer sphere

Let us be specific about the macroscopic body. Consider a sphere consisting of L concentric layers, each having permittivity $\epsilon_i(\omega)$, i running from 1 to L starting from the outermost layer, as sketched in Fig. 1. The spherical surfaces have radii $R_j(j=1,2,\cdots,L-1)$. The Green tensor of such a system can be found in Ref. [16]. We assume that the emitter is located in the core sphere, i.e., in layer L.

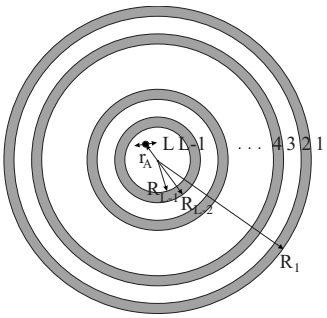

FIG. 1. A dipole emitter embedded in a multilayer sphere.

1. Decay rate

Putting the relevant Green tensor [16] in Eq. (15), we obtain

$$\Gamma^{(1)\perp} = \frac{3\Gamma_0}{2}\,\mathrm{Re}\left[\left(\frac{3\varepsilon_L}{2\varepsilon_L+1}\right)^2 \sum_{n=1}^{\infty} n(n+1)(2n+1) \times C_{Nn}^{LL}\left(\frac{j_n(k_L r_A)}{k_L r_A}\right)^2\right], \tag{18}$$

$$\Gamma^{(1)\parallel} = \frac{3\Gamma_0}{2}\,\mathrm{Re}\left\{\left(\frac{3\varepsilon_L}{2\varepsilon_L+1}\right)^2 \sum_{n=1}^{\infty} \frac{(2n+1)}{2} \times \left[C_{Nn}^{LL}\left(\frac{J_n'(k_L r_A)}{k_L r_A}\right)^2 + C_{Mn}^{LL} j_n^2(k_L r_A)\right]\right\} \tag{19}$$

for radially and tangentially oriented dipole moment, respectively.

2. Emission pattern in the far zone

We choose a spherical coordinate system with its origin coinciding with the center of the sphere and its z axis passing through the position of the emitter ($\theta_A=\phi_A=0$). To calculate the emission pattern in the far zone, we fix the field point (r,θ,ϕ) in the outermost layer 1. Then the vector $\mathbf{F}(\mathbf{r},\mathbf{r}_A,\omega_A)$ which determines the spatial distribution of emitted light according to Eqs. (2) and (16) is given by

$$\mathbf{F}^{\perp}(\mathbf{r},\mathbf{r}_A,\omega_A) = \frac{k_A^3 d_A}{4\pi\epsilon_0}\frac{3\varepsilon_L^{3/2}}{2\varepsilon_L+1}\sum_{n=1}^{\infty}\frac{A_{Nn}^{1L}(2n+1)}{k_1 r k_L r_A} j_n(k_L r_A) \times [\mathbf{e}_r n(n+1) h_n^{(1)}(k_1 r) P_n - \mathbf{e}_\theta H_n'(k_1 r)\sin\theta P_n'], \tag{20}$$

$$\mathbf{F}^{\parallel}(\mathbf{r},\mathbf{r}_A,\omega_A) = \frac{k_A^3 d_A}{4\pi\epsilon_0}\frac{3\varepsilon_L^{3/2}}{2\varepsilon_L+1}\sum_{n=1}^{\infty}(2n+1)\left\{\mathbf{e}_r\frac{A_{Nn}^{1L}}{k_1 r k_L r_A} J_n'(k_L r_A) h_n^{(1)}(k_1 r) P_n' \sin\theta\cos\phi + \mathbf{e}_\theta\frac{\cos\phi}{n(n+1)}\left[A_{Mn}^{1L} j_n(k_L r_A) h_n^{(1)}(k_1 r) P_n' + \frac{A_{Nn}^{1L}}{k_1 r k_L r_A} J_n'(k_L r_A) H_n'(k_1 r) Q_n\right] - \mathbf{e}_\phi\frac{\sin\phi}{n(n+1)}\left[A_{Mn}^{1L} j_n(k_L r_A) h_n^{(1)}(k_1 r) Q_n + \frac{A_{Nn}^{1L}}{k_1 r k_L r_A} J_n'(k_L r_A) H_n'(k_1 r) P_n'\right]\right\} \tag{21}$$

for radially and tangentially oriented dipole moment, respectively.

In Eqs. (18)–(21), all information about the geometry and material properties of the sphere is contained in the generalized reflection coefficients C_{Nn}^{LL}, C_{Mn}^{LL} and the generalized transmission coefficients A_{Nn}^{1L} and A_{Mn}^{1L}. They are to be determined via recurrence relations [16] with the subscript $N(M)$ indicating contributions from TM (TE) waves and the first (second) superscript indicating the layer where the field (source) point is located; $k_i=\sqrt{\varepsilon_i(\omega_A)}\omega_A/c$; $j_n(z)$ and $h_n^{(1)}(z)$ denote the spherical Bessel functions and the spherical Hankel functions of the first type, respectively; $P_n \equiv P_n(\cos\theta)$ denotes the Legendre polynomials;

$$J_n'(z) = \frac{d[z j_n(z)]}{dz}, \tag{22}$$

$$H_n'(z) = \frac{d[z h_n^{(1)}(z)]}{dz}; \tag{23}$$

and

$$Q_n = \cos\theta P_n' - \sin^2\theta P_n'' = n(n+1)P_n - \cos\theta P_n'. \tag{24}$$

It can be seen from Eqs. (18)–(21) that a radially oriented dipole moment interacts with only TM waves while a tangentially oriented dipole moment interacts with both TM and TE waves. Equations (20) and (21) for the emission patterns hold for an arbitrary distance from the multilayer sphere. Using the large-argument expansions [27]

$$h_n^{(1)}(z) \sim \frac{1}{z} e^{i(z-n\pi/2-\pi/4)}, \tag{25}$$

$$H_n'(z) \sim i e^{i(z-n\pi/2-\pi/4)}, \tag{26}$$

it can be inferred that in the far zone, the radial component $\mathbf{e}_r$ vanishes while the transverse components $\mathbf{e}_\theta$ and $\mathbf{e}_\phi$ survive, as they should.

3. Energy flow through a surface

With a discussion of the output coupling efficiency in mind, we calculate the radiation energy transported through an area located in the core layer. Using the relevant Green

tensor [16] in Eqs. (17) and (7), and assuming that the transition dipole moment is oriented in the radial direction, we obtain the following expression for the radiation energy emitted per unit solid angle:

$$\frac{W^{\perp}(\Omega)}{W_0} = \frac{\Gamma_0}{\Gamma^{\perp}} \frac{3k_A r}{8\pi} \left| \frac{3\varepsilon_L}{2\varepsilon_L + 1} \right|^2 \mathrm{Im}(\varepsilon_L A_{\theta}^{*} B_{\phi}), \tag{27}$$

where $W_0 = \hbar\omega_A$ is the total available energy and

$$A_{\theta} = -\sum_{n=1}^{\infty} (2n+1) \frac{j_n(k_L r_A)}{k_L r_A} [H_n'(k_L r) + C_{Ln}^{LL} J_n'(k_L r)] \sin\theta P_n', \tag{28}$$

$$B_{\phi} = \sum_{n=1}^{\infty} (2n+1) \frac{j_n(k_L r_A)}{k_L r_A} [h_n(k_L r) + C_{Ln}^{LL} j_n(k_L r)] \sin\theta P_n' \tag{29}$$

arise from the θ component of $\mathbf{G}_{\mathrm{med}}\mathbf{d}_A$ and the ϕ component of $\boldsymbol{\nabla} \times (\mathbf{G}_{\mathrm{med}}\mathbf{d}_A)$, respectively.

Also of interest is the amount of radiative energy transmitted to the far zone. Substituting Eqs. (20) and (2) into Eq. (8) and performing the integrals, we obtain

$$\frac{W^{\perp}}{W_0} = \frac{3\Gamma_0}{2\Gamma^{\perp}} \sum_{n=1}^{\infty} n(n+1)(2n+1) \left| \frac{3\varepsilon_L}{2\varepsilon_L + 1} \frac{A_{Nn}^{1L} j_n(k_L r_A)}{k_1 r_A} \right|^2. \tag{30}$$

The tangentially oriented-dipole-moment counterparts of Eqs. (27)–(30) are very cumbersome and we renounce from giving them here.

4. Atom on center

For an emitter positioned at the center of a multilayer sphere ($r_A = 0$), the distinction between different dipole moment orientations becomes meaningless. Using [27]

$$j_n(z)|_{z\to 0} \simeq \frac{z^n}{(2n+1)!!}, \tag{31}$$

it is not difficult to see that in Eqs. (18)–(21) and (28)–(30), only ($n=1$) terms contribute [15,24], resulting in

$$\Gamma^{(1)} = \Gamma_0 \,\mathrm{Re}\left[\left(\frac{3\varepsilon_L}{2\varepsilon_L + 1} \right)^2 C_{N1}^{LL} \right] \tag{32}$$

for the decay rate

$$\mathbf{F}(\mathbf{r}, r_A = 0, \omega_A) = -\frac{k_A^3 d_A}{4\pi\epsilon_0} \frac{3\varepsilon_L^{3/2}}{2\varepsilon_L + 1} A_{N1}^{1L} \frac{e^{ik_1 r}}{k_1 r} \left[\mathbf{e}_r 2 \left(\frac{i}{k_1^2 r^2} + \frac{1}{k_1 r} \right) \cos\theta + \mathbf{e}_{\theta} \left(\frac{i}{k_1^2 r^2} + \frac{1}{k_1 r} - i \right) \sin\theta \right], \tag{33}$$

where the emitter dipole oscillates along the z axis, for the emission pattern,

$$\frac{W(\Omega)}{W_0} = -\frac{\Gamma_0}{\Gamma} \frac{3k_A r}{8\pi} \sin^2\theta \left| \frac{3\varepsilon_L}{2\varepsilon_L + 1} \right|^2 \mathrm{Im}\{\varepsilon_L [H_1'(k_L r) + C_{N1}^{LL} J_1'(k_L r)]^{*} [h_1(k_L r) + C_{N1}^{LL} j_1(k_L r)]\} \tag{34}$$

for the radiation energy emitted per unit angle and

$$\frac{W}{W_0} = \frac{\Gamma_0}{\Gamma} \left| \frac{3\varepsilon_L^{3/2}}{2\varepsilon_L + 1} \frac{A_{N1}^{1L}}{\sqrt{\varepsilon_1}} \right|^2 \tag{35}$$

for the total amount of energy transported to the far zone. From Eqs. (33) and (2), it can be seen that when the dipole emitter is located at the center of the sphere, the intensity of the radiation field in the far zone is proportional to $\sin^2\theta$, the same angle dependence as that for a dipole emitter located in free space [24]. This is independent of the emitter transition frequency and can be explained as being due to the central position of the emitter and the spherical symmetry of the system.

III. SPONTANEOUS DECAY -NUMERICAL RESULTS

The formulas presented in the previous section hold for an arbitrary configuration of concentric spheres. We are interested in structures where layers from 2 to $L-1$ have interchanging high permittivity $\varepsilon_{\mathrm{high}}$ and low permittivity $\varepsilon_{\mathrm{low}}$ and quarter-wavelength optical thicknesses $d_j = \lambda_0/[4\mathrm{Re}\sqrt{\varepsilon_j(\omega_0)}]$ ($\lambda_0 \equiv 2\pi c/\omega_0$, where ω_0 is the midgap frequency). In the numerical calculations we set $\varepsilon_L(\omega) \simeq \varepsilon_{\mathrm{low}}(\omega) \simeq 1$, $\varepsilon_1(\omega) = 1$, and assume that $\varepsilon_{\mathrm{high}}(\omega)$ can be modeled by a single-resonance permittivity of Drude-Lorentz type

$$\epsilon_{\mathrm{high}}(\omega) = 1 + \frac{\omega_P^2}{\omega_T^2 - \omega^2 - i\omega\gamma}, \tag{36}$$

where ω_P is the plasma frequency and ω_T and γ are, respectively, the transverse resonance frequency of the medium and the linewidth of the associated absorption line.

Since the decay rate is proportional to the density of states of the medium-assisted electromagnetic field at the position of the emitter, a plot of the first also demonstrates the behavior of the latter. Figure 2 gives examples of how the decay rate of an emitter placed at the center of the sphere, Eqs. (12)–(14) and (32), varies with respect to the emitter transition frequency for different numbers of layers. As the number of layers increases, the band gap, already visible at $L=7$ (the corresponding number of layers in the shell is 5), becomes more and more distinct and the resonances within the band gap grow sharper. These resonances are essentially defect resonances related to the presence of the core sphere. The quality factor Q, determined as $Q = \omega/(2\delta)$, ω and δ being the position and the half width at half maximum of a resonance, of the fundamental resonances in Fig. 2 is approximately 6×10^2 for $L=7$, 10^7 for $L=21$, and 6×10^{10} for $L=35$. Advantages of spherical Bragg-distributed resonators, which provide a three-dimensional confinement of the electromagnetic field, over planar ones, which confine the electromagnetic field in only one dimension, are clearly seen in Fig. 2: the maximum degrees of spontaneous decay enhance-

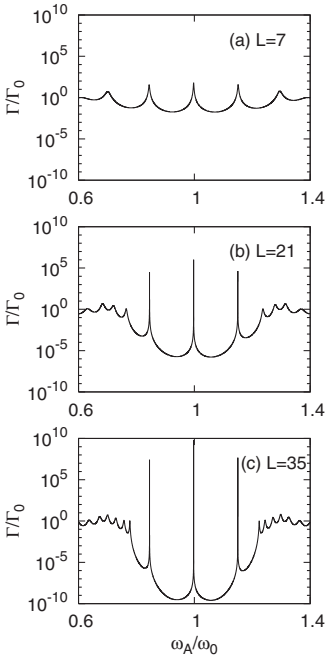

FIG. 2. Frequency dependence of the normalized decay rate of an emitter placed at the sphere center for configurations of different numbers of layers. The parameters are $\epsilon_L \simeq \epsilon_{\text{low}} \simeq 1$, $\epsilon_1 = 1$, ϵ_{high} given as in Eq. (36) with $\omega_P = 1.7299\omega_T$, $\omega_T = 20\omega_0$, and $\gamma = 10^{-7}\omega_0$; and the radius of the core sphere $R_{L-1} = 3\lambda_0$.

ment and suppression achievable in the first are drastically higher than those achievable in the latter. The normalized decay rate Γ/Γ_0 can take on values as low as $\sim 10^{-9}$ at the dips and as high as $\sim 10^{10}$ at the peaks in resonators of the spherical type [see Fig. 2(c)], while for similar number of layers and values of permittivities, the corresponding values in resonators of the planar type are only ~ 0.2 and ~ 2.5, respectively [9]. Note that the fundamental resonance of a spherical Bragg-distributed resonator is not necessarily located at the frequency ω_0. In Fig. 2, they are slightly below the midgap frequency. In contrast to the case of planar Bragg-distributed resonators, resonance frequencies in spherical Bragg-distributed resonators vary, albeit by only very small amounts, with varying number of layers. For example, frequencies of the central resonances in Fig. 2 are $0.9974684\omega_0$, $0.9974813117\omega_0$, and $0.997481312380\omega_0$ for $L=7$, 21, and 35, respectively (see also Ref. [14]).

Figure 3 illustrates how the decay rate, Eqs. (12)–(14), (18), and (19), behaves as the emitter is moved across a radius of the core sphere. In Figs. 3(a) and 3(b), the emitter position is varied along the y axis while its transition frequency is varied along the x axis. The decay rates are mapped upon the xy plane. We restricted ourselves to configurations of seven layers to keep down the sizes of the data files. It can be seen that there exist a number of field resonance peaks. In similarity with the whispering gallery resonances, which originate from the total internal reflection and concentrate near the boundaries [28], the resonances can be classified by three indices: the angular momentum number n, the azimuthal number m, and the number i of radial maxima of the field in the core sphere, with $2n+1$ azimuthal reso-

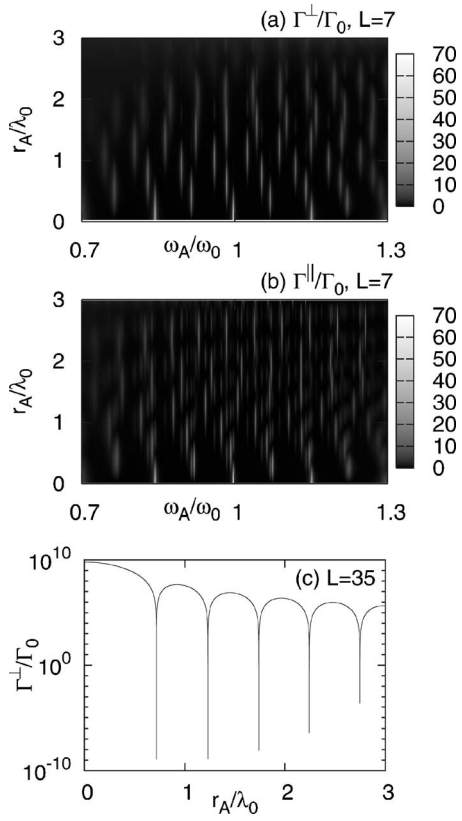

FIG. 3. Position dependence of an emitter decay rate. (a) The emitter dipole moment is radially oriented. (b) The emitter dipole moment is tangentially oriented. In (a) and (b), the parameters are the same as in Fig. 2(a). (c) The emitter transition frequency is fixed at a resonance frequency $\omega_A/\omega_0 = 0.997481312380$. The parameters are the same as in Fig. 2(c).

nances being degenerate when the spheres are uniform. The resonances at the sphere center have $n=1$, while those having larger n start to appear as the emitter is moved off center. The angular momentum numbers of the most pronounced resonances in a spherical Bragg-distributed resonator are usually small, which is different from the whispering gallery resonances, whose angular momentum numbers are typically large [28]. The resonances with smaller n tend to be of higher Q than those having larger n. In the case of a tangentially oriented dipole moment, more resonances occur than in the case of a radially oriented one. This is because the first is coupled to both TM and TE waves, while the latter is coupled only to TM waves [see Eqs. (18) and (19)].

Figure 3(c) shows the position dependence of the sharpest field resonance in a 35-layer configuration. Though the highest peak in space occurs at the sphere center, significant peaks persist right up to the boundary. Note that when the emitter transition frequency coincides with a resonance frequency, the dominant contribution to the sum comes from the term having n equal to the angular momentum number of that resonance.

Figure 4 shows the decay rate of an emitter placed at the sphere center as a function of the core sphere radius and the emitter transition frequency. As the radius increases, the number of resonances within the band gap increases, their

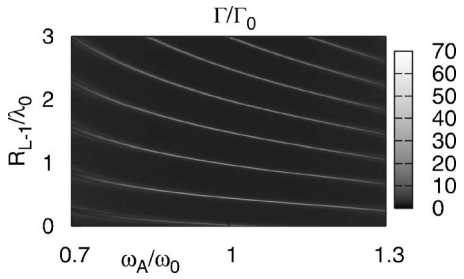

FIG. 4. The dependence of the decay rate on the size of the core sphere and the emitter transition frequency for a seven-layer configuration. The emitter is placed at the sphere center. Other parameters are the same as in Fig. 2(a).

spectral lines moving across the band gap from the higher-frequency side to the lower-frequency side, and their quality factors being, in general, improved. Interestingly, a resonance survives even as the diameter of the core sphere is smaller than a half wavelength, which is different from the case of planar resonators where no resonance exists for cavity sizes smaller than a half wavelength.

We turn now to the emission pattern of an emitter enclosed within a spherical band-gap structure. We restrict ourselves to the simpler case of a radially oriented dipole moment. When the emitter is on resonance, the dominant contribution arises from the n term, n being the angular momentum number of that resonance. Hence the angular distribution of the radiated field in the far zone is determined roughly by $-\sin\theta P_n'(\cos\theta)=P_n^1(\cos\theta)$. This fact leads to two important consequences. First since $|P_n^1[\cos(\pi-\theta)]|=|P_n^1[\cos(\theta)]|$ [27], the emission pattern is symmetric with respect to the $(z=0)$ plane independently of the emitter position. When $n=1$, due to $P_n'(\cos\theta)=1$, the far-field emission

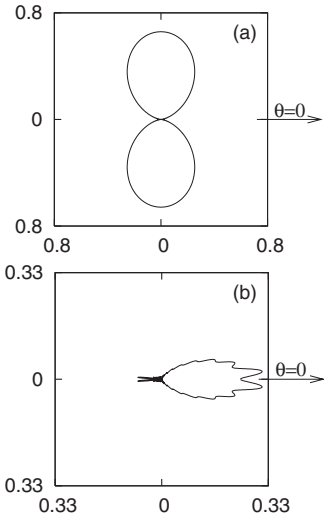

FIG. 5. Polar diagram of the normalized far-field emission pattern of a radially oriented emitter dipole moment for $r_A=2.95\lambda_0$ and $r=80\lambda_0$. (a) $|\mathbf{F}(\mathbf{r},\mathbf{r}_A,\omega_A)|^2/(k_A^3 d_A/4\pi\epsilon_0)^2$ for the on-resonance case $\omega_A/\omega_0=0.997481312380$ and (b) $10^6\times|\mathbf{F}(\mathbf{r},\mathbf{r}_A,\omega_A)|^2/(k_A^3 d_A/4\pi\epsilon_0)^2$ for the off-resonance case $\omega_A/\omega_0=0.99748$. Other parameters are the same as in Fig. 2(c).

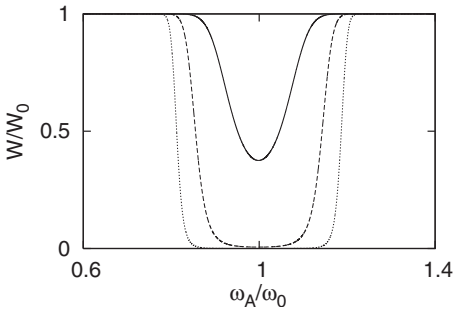

FIG. 6. The amount of radiation energy W observed outside the resonator, Eq. (35), as a function of the emitter transition frequency for an emitter placed at the sphere center and for $\gamma/\omega_0=10^{-7}$ (solid line), 10^{-5} (dashed line), and 10^{-3} (dotted line). Other parameters are the same as in Fig. 2(c).

intensity is proportional to $\sin^2(\theta)$, similar to that in free space. This holds not only for an atom placed at the sphere center, as we already mentioned below Eq. (35), but also for an atom placed off center, as pictured in Fig. 5(a) in accordance with Eq. (20). Second, since $P_n(\cos\theta)$ is a polynomial with n real, single roots in the interval $0<\theta<\pi$, $\sin\theta P_n'(\cos\theta)$ must have n extrema within the same interval. Thus, the emission pattern has n lobes in, say, the yz plane, i.e., n cone-shaped peaks around the z axis. Note that in spherical band-gap structures, the most pronounced resonances are well separated in frequency, preserving the symmetry of the emission pattern between the forward $(\theta<\pi/2)$ and backward $(\theta>\pi/2)$ directions. In whispering gallery resonance structures, resonances have large n and tend to overlap. As a consequence, superposition of the leading n term with the remaining terms in the sums gives rise to some asymmetry with respect to the $(\theta=\pi/2)$ plane [24]. When the emitter is off resonance with the medium-assisted electromagnetic field, multiple terms contribute more or less equally, resulting in a complex emission pattern, an example of which is given in Fig. 5(b).

Figure 6 shows the spectral dependence of the amount of radiation energy observed outside the structure for various degrees of material absorption. A value of the ratio W/W_0 close to one means that most of the available energy reaches the outside of the resonator, while a value close to zero means that most of the emitted energy is absorbed by the media surrounding the emitter. The figure reveals that on resonance or off, within the band gap, nonradiative decay dominates. This is because within the band gap, the emitted photon is captured for sometime inside the structure and has a high probability of being absorbed. The larger the degree of material absorption, the higher this probability.

IV. SINGLE-PHOTON GENERATION

In practice, a dipole emitter can be an atom, ion, molecule, semiconductor quantum dot, nanocrystal, or nitrogen vacancy center. It can be introduced into the core layer by sparse doping or implanting. Depending on the energy level configuration of the emitter, a suitable pumping mechanism

can be chosen. Examples include the 1.55 μm $^4I_{13/2}\rightarrow{}^4I_{15/2}$ transition of the Er^{3+} ion, which is convenient for quantum communication with optical fibers and can be pumped via stimulated Raman adiabatic passage [29] with a 100% guarantee of population transfer. For four-level schemes with fast nonradiative decays between the two upper and the two lower states as in the case of nitrogen vacancy centers or dye molecules, nonresonant pumping can be employed [2]. Note that a spherical Bragg-distributed resonator supports multiple well isolated resonances, some of which can be used to convey the external laser fields that drive the pumping process. After being excited, the emitter is left in the upper state for a time inversely proportional to that state's lifetime. As can be inferred from the discussion in the previous section, this lifetime can be extremely short if the emitter transition frequency coincides with a resonance frequency of a spherical Bragg-distributed resonator. This very narrow emission time window makes the source deterministic. Note that the determinicity of a source depends not only on the determinicity of the emission process, but on that of the excitation procedure as well. The photon generation is called "on-demand" because the onset of the spontaneous decay is externally controllable.

In spherical distributed resonators, large spontaneous emission enhancement factors on resonance and strong spontaneous emission suppression off it ensure that the fraction of spontaneous emission coupled into a single desired mode is very close to unity. The next question is how to collect this emission to make it useful with a high efficiency. In previously proposed schemes based on photonic band-gap materials with periodically varying refractive index, a single-mode coupling and output channel are realized via a waveguide in a 2D photonic crystal that is embedded in a 3D photonic band-gap material [2,8]. Here, we propose an output channel in the form of an optical fiber attached to the spherical resonator. In a modal analysis of Bragg onion resonators where a stem is present instead of a fiber, it has been shown that the presence of a stem does not substantially affect the fraction of the spontaneous emission that goes into the desired mode, provided that stem radius is much smaller than the radius of the core sphere [19]. Similarly, if the fiber is only weakly coupled to the resonator, i.e., if its radius r_f is much smaller than that of the core sphere R_{L-1}, the single-mode emission factor should remain close to unity. Let us estimate now the amount of energy transported through the contact area $\mathcal{A}$ of the fiber with the core sphere. Substituting Eq. (34) into Eq. (6) and positioning the area $\mathcal{A}$ at $\theta=\pi/2$, we obtain

$$\frac{W_{\mathcal{A}}}{W_0} \simeq \frac{3}{2\pi}\left|\frac{3\varepsilon_L}{2\varepsilon_L+1}\right|^2\sqrt{\varepsilon_L}\left(\frac{r_f}{R_{L-1}}\right)^2, \tag{37}$$

where it has been assumed for transparency that the emitter is located at the sphere center, the material absorption in the core layer can be neglected, and that $r_f \ll R_{L-1}$. For, say, $r_f/R_{L-1}\sim 0.1$ (a typical value of r_f of a single-mode fiber designed for use in the near infrared is about 4–5 μm), $W_{\mathcal{A}}/W_0$ takes on the value of ~ 0.01. This is the same as collection efficiencies in sources where no Purcell effect is employed [1]. If all the radiation incident upon $\mathcal{A}$ is within the numerical aperture of the fiber, one might, in a sense, regard the quantity $W_{\mathcal{A}}/W_0$ calculated in the above manner as some kind of lower bound for the collection efficiency of the single-photon source. We note, however, that the result (37) has been derived using the Green tensor of a closed sphere. Recalling planar geometries of unbalanced mirrors, in which emitted light emerges chiefly via the mirror of lesser reflectivity [9], it can be expected that when an output channel in the form of an optical fiber is present, the emission is directed primarily into the output channel where no blocking wall is present. Hence the output coupling efficiency can be much higher than that given in Eq. (37). The concentration of the emitted light in the direction of the output channel can be interpreted in the following way. Let us for simplicity place the atom at the sphere center. The emitted photon, if not incident upon the fiber right away, will bounce back and forth within the reflecting wall, changing direction via being scattered by the atom until finally reaching the output channel.

In studies of the whispering gallery resonances [30], microspheres have been produced by heat-fusing the tips of thin silica wires or fibers with a CO_2 laser or a microtorch. The spheres are formed at the ends of the fibers under the effect of surface tension with diameters in the range 40–300 μm, about three to ten times the initial fibers' thickness. On the other hand, mode structures of the so-called Bragg onion resonators have been analyzed [19]. The onionlike resonators consisting of a spherical air core bound by Bragg cladding pairs composed of SiO_2 and Si are fabricated through a combination of etching and chemical-vapor deposition. These lead us to the suggestion that our system might be materialized in three stages: The core sphere plus the output channel is produced along the lines given in Ref. [30], followed by the core sphere being coated with Bragg cladding layers via chemical-vapor deposition as in Ref. [19]. The emitter, depending on a particular choice, can be deposited in the core layer before or after the fusion step using an appropriate method.

The effects of material absorption on the quality factor of the field resonances, hence the emitter upper-state lifetime, are illustrated in Fig. 8 (see solid lines). For $\gamma/\omega_0=10^{-7}$, the quality factor is equal to $Q\sim 6\times 10^{10}$ [cf. central peak in Fig. 2(c)]. As γ/ω_0 increases from 10^{-5} to 10^{-1}, which corresponds to an increase of $\mathrm{Im}\varepsilon_{\mathrm{high}}$ from $\sim 7.5\times 10^{-8}$ to $\sim 7.5\times 10^{-4}$, the quality factor of the central resonances in Fig. 8 decreases from about 10^9 to about 10^5.

Due to fabrication imperfections, it would be too demanding to require that the thicknesses of the layers stick rigorously to designated values. The effects of layer-thickness deviation from a quarter wavelength on the band-gap structure, resonance positions and widths are explored in Fig. 9(a). When the magnitude of the deviation increases, the bottom of the band gap gets more shallow and the band gap gradually disappears, but sharp resonances can still survive, albeit with reducing quality factors. Resonance with quality factor as high as 8×10^4 can be found despite a layer thickness randomization of up to 70% of a quarter wavelength, that is, $\lambda_0/[4\mathrm{Re}\sqrt{\varepsilon_j(\omega_0)}]$, $j=2,3,\ldots,L$. The existence of high-quality resonances in spherical Bragg-distributed resonators

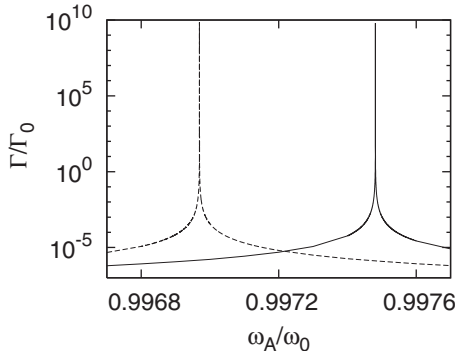

FIG. 7. The spectral shift of a field resonance due to a switch of $\varepsilon_{\text{high}}$ from $\sim 4+i7.5\times10^{-10}$ ($\omega_P=1.7299\omega_T$, solid line), to $\sim 4.0840+i7.7\times10^{-10}$ ($\omega_P=1.7529\omega_T$, dashed line). Other parameters are the same as in Fig. 2(c).

is thus very robust against irregularities in the layer thicknesses.

Additional flexibility, for example, a separation of the excitation and emission process, can be achieved by first exciting the emitter off resonance, then shifting the field resonance frequencies to make one of them coincide with the emitter transition frequency, thereby causing a fast spontaneous decay accompanied by a photon emission. The shift can be implemented, say, by tuning the refractive index of the structure backbone. This can be materialized via embedding a material with intensity-dependent Kerr-nonlinear refractive index in the structure backbone and shining an external laser pulse on it [8,9]. Figure 7 shows the spectral profile of the fundamental resonance in a 35-layer system [central peak in Fig. 2(c)] before (solid line) and after (dashed line) the switch. Thus if we choose an emitter with a transition frequency that lies away from the resonance frequency represented by the solid line in Fig. 7 and coincides with the resonance frequency represented by the dashed line, when the emitter is excited, its spontaneous decay is first inhibited ($\Gamma/\Gamma_0\sim10^{-9}$ for the parameters used) and the emitter stays in the upper state due to the extremely low density of the available field states. Once an external laser pulse is turned on, the emitter transition frequency falls into resonance with the medium-assisted electromagnetic field and the spontaneous decay takes place almost instantaneously ($\Gamma/\Gamma_0\sim10^{10}$).

Visually, for the Kerr-switching scheme to work, a strong spontaneous decay suppression (enhancement) before (after) the switch at the resonance frequency shown by the dashed line in Fig. 7 is required. Material absorption, characterized by γ in the Drude-Lorentz model (36), leads to nonradiative decay and the emitted photon being lost. The effects of the material absorption on the decay rate are illustrated in Fig. 8. For the parameters used, the scheme is still feasible at $\gamma/\omega_0=10^{-3}$ ($\text{Im}\varepsilon_{\text{high}}\sim7.5\times10^{-6}$) with a spontaneous decay suppression before the switch of $\Gamma/\Gamma_0\sim10^{-2}$ and a spontaneous decay enhancement after the switch of $\Gamma/\Gamma_0\sim10^{6}$, but no longer works at $\gamma/\omega_0=10^{-1}$ ($\text{Im}\varepsilon_{\text{high}}\sim7.5\times10^{-4}$).

Figure 9(b) shows the effects of the deviation of the layer thicknesses from the desired quarter-wavelength values on the feasibility of the Kerr-switching scheme. The figure reveals that even with a thickness randomization of up to

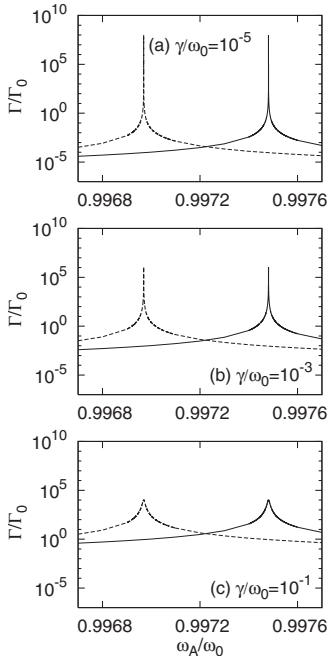

FIG. 8. Effects of material absorption on a field resonance before (solid line) and after (dashed line) the switch. Other parameters are the same as in Fig. 7.

$0.7\lambda_0/[4\text{Re}\sqrt{\varepsilon_j(\omega_0)}]$ in layer j, one still can pick up a resonance for which the degree of spontaneous decay suppression before the switch and the degree of spontaneous decay enhancement on-resonance after the switch are $\Gamma/\Gamma_0\sim10^{-2}$ and 10^4, respectively, values which still allow for a Kerr-switching scheme to work. That is to say, the scheme is very robust against irregularities in the layer thicknesses.

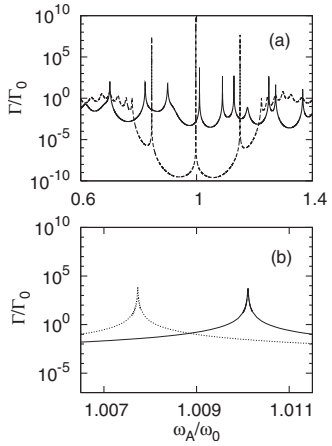

FIG. 9. Effects of layer-thickness irregularities of up to ±70% of the quarter wavelength ($\pm0.7\lambda_0/[4\text{Re}\sqrt{\varepsilon_j(\omega_0)}]$) in layer j ($j=2,3,\ldots,L$). (a) The emitter spontaneous decay rate in a structure with perfect quarter-wavelength layer thicknesses (dashed line) and that in a structure containing layer-thickness irregularities (solid line). (b) A field resonance in a structure containing layer-thickness irregularities before (solid line) and after (dotted line) a Kerr-nonlinearity switch. Other parameters are the same as in Fig. 7.

V. SUMMARY

We have investigated various characteristics of the spontaneous decay process of a dipole emitter enclosed within a spherical Bragg-distributed resonator, including the decay rates, the emission pattern, and the amount of radiation energy in the far zone, with emphasis on aspects relevant to our discussion on the design of a single-photon source. Comparisons with whispering gallery resonance and planar systems have been made.

We have shown that a system of a dipole emitter enclosed in a spherical Bragg-distributed resonator, equipped with an output channel in the form of an optical fiber, is a very promising candidate for an on-demand and deterministic single-photon source. The presence of well separated in frequency, high-Q resonances facilitates a single-resonance emitter-field coupling and shortens the emitter upper state lifetime, thereby helping to improve the determinicity of the source.

A more sophisticated scheme has been suggested by employing a Kerr-nonlinear material that allows one to tune the band gap externally. Energy is pumped in and stored in the emitter by first exciting it off-resonance. The release of a photon is triggered by applying a laser pulse that tunes a field resonance to the emitter transition frequency.

We have shown that both schemes are robust against material absorption and irregularities in the layer thicknesses. Although factors such as a deformation of the sphere or the presence of the output coupling structure, whose analytical analysis is difficult, might lead to a broadening of the field resonance lines, we believe they will not render the proposed schemes useless. Compared with three-dimensional photonic crystals, spherical Bragg-distributed structures offer many advantages in design simplicity and practical fabrication process.

ACKNOWLEDGMENTS

We thank the Ho Chi Minh city National University and the National Program for Basic Research of Vietnam for funding. H.T.D. acknowledges support from the Abdus Salam International Centre for Theoretical Physics, where part of this work was carried out.

[1] W. L. Barnes, G. Björk, J. M. Gérard, P. Jonsson, J. A. E. Wasey, P. T. Worthing, and V. Zwiller, Eur. Phys. J. D **18**, 197 (2002).
[2] M. Oxborrow and A. G. Sinclair, Contemp. Phys. **46**, 173 (2005).
[3] F. De Martini, G. Di Giuseppe, and M. Marrocco, Phys. Rev. Lett. **76**, 900 (1996).
[4] S. C. Kitson, P. Jonsson, J. G. Rarity, and P. R. Tapster, Phys. Rev. A **58**, 620 (1998).
[5] E. Moreau, I. Robert, J. M. Gérard, I. Abram, L. Manin, and V. Thierry-Mieg, Appl. Phys. Lett. **79**, 2865 (2001).
[6] C. Santori, D. Fattal, J. Vuckovic, G. S. Solomon, and Y. Yamamoto, New J. Phys. **6**, 89 (2004).
[7] M. Keller, B. Lange, K. Hayasaka, W. Lange, and H. Walther, New J. Phys. **6**, 95 (2004).
[8] M. Florescu, S. Scheel, H. Häffner, H. Lee, D. V. Strekalov, P. L. Knight, and J. P. Dowling, Europhys. Lett. **69**, 945 (2005).
[9] Ho Trung Dung, L. Knöll, and D.-G. Welsch, Phys. Rev. A **67**, 021801(R) (2003); **69**, 063811 (2004).
[10] J. Q. You, Y.-X. Liu, C. P. Sun, and F. Nori, Phys. Rev. B **75**, 104516 (2007).
[11] J. Laurat, H. Riedmatten, D. Felinto, C.-W. Chou, E. W. Schomburg, and H. J. Kimble, Opt. Express **14**, 6912 (2006); D. N. Matsukevich, T. Chanelière, S. D. Jenkins, S.-Y. Lan, T. A. B. Kennedy, and A. Kuzmich, Phys. Rev. Lett. **97**, 013601 (2006); S. Chen, Y.-A. Chen, T. Strassel, Z.-S. Yuan, B. Zhao, J. Schmiedmayer, and J.-W. Pan, *ibid.* **97**, 173004 (2006).
[12] T. B. Pittman, B. C. Jacobs, and J. D. Franson, Phys. Rev. A **66**, 042303 (2002); E. Jeffrey, N. A. Peters, and P. G. Kwiat, New J. Phys. **6**, 100 (2004).
[13] D. Brady, G. Papen, and J. E. Sipe, J. Opt. Soc. Am. B **10**, 644 (1993).
[14] G. Burlak, S. Koshevaya, J. Sanchez-Mondragon, and V. Grimalski, Opt. Commun. **180**, 49 (2000); **187**, 91 (2001).
[15] M. A. Kaliteevski, S. Brand, R. A. Abram, and V. V. Nikolaev, J. Mod. Opt. **48**, 1503 (2001).
[16] L. W. Li, P. S. Kooi, M. S. Leong, and T. S. Yeo, IEEE Trans. Microwave Theory Tech. **42**, 2302 (1994).
[17] A. Moroz, Ann. Phys. (N.Y.) **315**, 352 (2005).
[18] C. Deumié, P. Voarino, and C. Amra, Appl. Opt. **41**, 3299 (2002).
[19] Y. Xu, W. Liang, A. Yariv, J. G. Fleming, and S.-Y. Lin, Opt. Lett. **29**, 424 (2004).
[20] I. Gourevich, L. M. Field, Z. Wei, C. Pachet, A. Petukhova, A. Alteheld, E. Kumacheva, J. J. Saarinen, and J. E. Sipe, Macromolecules **39**, 1449 (2006).
[21] R. Takekoh, W.-H. Li, N. A. D. Burke, and H. D. H. Stöver, J. Am. Chem. Soc. **128**, 240 (2006).
[22] K. G. Sullivan and D. G. Hall, Phys. Rev. A **50**, 2701 (1994); **50**, 2708 (1994).
[23] G. S. Agarwal, Phys. Rev. A **12**, 1475 (1975); J. M. Wylie and J. E. Sipe, *ibid.* **30**, 1185 (1984).
[24] Ho Trung Dung, L. Knöll, and D.-G. Welsch, Phys. Rev. A **62**, 053804 (2000).
[25] M. S. Tomaš, Phys. Rev. A **63**, 053811 (2001).
[26] Ho Trung Dung, S. Y. Buhmann, and D.-G. Welsch, Phys. Rev. A **74**, 023803 (2006).
[27] *Handbook of Mathematical Functions*, edited by M. Abramowitz and I. A. Stegun (Dover, New York, 1973).
[28] Ho Trung Dung, L. Knöll, and D.-G. Welsch, Phys. Rev. A **64**, 013804 (2001).
[29] K. Bergmann, H. Theuer, and B. W. Shore, Rev. Mod. Phys. **70**, 1003 (1998).
[30] V. B. Braginsky, M. L. Gorodetsky, and V. S. Ilchenko, Phys. Lett. A **137**, 393 (1989); L. Collot, V. Lefèvre-Seguin, M. Brune, J. M. Raimond, and S. Haroche, Europhys. Lett. **23**, 327 (193).